

Spacecraft Thermal And Optical Modeling Impacts on Estimation Of The GRAIL Lunar Gravity Field

Eugene G. Fahnestock*, Ryan S. Park†, Dah-Ning Yuan‡ and Alex S. Konopliv§
Jet Propulsion Laboratory, California Institute of Technology, Pasadena, CA, 91101, USA

We summarize work performed involving thermo-optical modeling of the two Gravity Recovery And Interior Laboratory (GRAIL) spacecraft. We derived several reconciled spacecraft thermo-optical models having varying detail. We used the simplest in calculating SRP acceleration, and used the most detailed to calculate acceleration due to thermal re-radiation. For the latter, we used both the output of pre-launch finite-element-based thermal simulations and downlinked temperature sensor telemetry. The estimation process to recover the lunar gravity field utilizes both a nominal thermal re-radiation acceleration history and an apriori error model derived from that plus an off-nominal history, which bounds parameter uncertainties as informed by sensitivity studies.

Nomenclature

A	area of plate surface, m^2
C_1	solar flux constant at 1 AU, $\text{kg m AU}^2/\text{m}^2/\text{s}^2$
C_d	diffuse reflectivity
C_s	specular reflectivity
G_X, G_Y	scale factors for SRP acceleration components normal to $\hat{\mathbf{r}}$
I_{sc}	short circuit current read from solar arrays bus controller
J	cost function
N	number of data points
P_{in}	power coming into spacecraft from the sun, W
P_{out}	power emitted from spacecraft, W
T	average surface temperature, or sensor temperature, K
V_{oc}	open circuit voltage read from solar arrays bus controller
$\hat{\mathbf{n}}$	outward-directed plate surface normal unit vector
$\hat{\mathbf{r}}$	unit direction vector from sun to spacecraft
\mathbf{A}_i	row of below mapping matrix
\mathbf{T}	vector of surface or sensor temperatures, K
\mathbf{a}_{srp}	acceleration on spacecraft due to solar radiation pressure (SRP), m/s^2
\mathbf{a}_{therm}	acceleration on spacecraft due to thermal radiation, m/s^2
\mathbf{z}	vector of residuals
A_{ij}	matrix for mapping from sensors to surfaces
c	speed of light in a vacuum, m/s
k, l	timestamp identifiers
k_2	degree 2 tidal Love number
$m_{S/C}$	spacecraft mass, kg
n, m	number of surfaces

*Navigation Engineer, Solar Systems Dynamics Group, 4800 Oak Grove Drive, Mail Stop 301-121, Lifetime Member AIAA.

†Gravity Science Analyst, Solar Systems Dynamics Group, 4800 Oak Grove Drive, Mail Stop 301-121, Senior Member AIAA.

‡Gravity Science Analyst, Solar Systems Dynamics Group, 4800 Oak Grove Drive, Mail Stop 301-121.

§Project Co-Investigator, Solar Systems Dynamics Group, 4800 Oak Grove Drive, Mail Stop 301-121.

©2012 California Institute of Technology. Government sponsorship acknowledged.

p	time-varying shadowing function for the spacecraft (1 out of shadow, 0 in umbra)
r_p	distance from the sun, AU
t	time, usually SCET or TDB timescale

Subscripts

i	plate surface identifier
j	temperature sensor identifier

Symbols

α	absorptivity
β	angle of the local sun direction away from the orbit plane
χ	skew-averaging parameter for material properties and thermal simulation cases = time since launch in years
ΔT	temperature bias, K
$\Delta \bar{C}_{21}, \Delta \bar{S}_{21}$	corrections to degree 2, order 1 normalized spherical harmonic coefficients, due to pole offset of core and mantle frames
ϵ	emissivity
μ	Orbit Determination Program specular reflectivity parameter
ν	Orbit Determination Program diffuse reflectivity parameter
ψ	time-varying solar incidence angle of plate surface
σ	standard deviation, or uncertainty
σ_{SB}	Stefan-Boltzmann constant, $5.6697 \times 10^{-8} \text{ W/m}^2/\text{K}^4$
ϕ	phase angle within orbit, measured from 0° = point in orbit at which sun-moon-s/c angle is minimized (hence equal to β)

I. Introduction

At the time of this writing, the Gravity Recovery And Interior Laboratory (GRAIL) has recently completed its originally planned three-month primary science mission. This involved formation flight of the two GRAIL spacecraft in low-altitude near-polar orbit about the moon for 89 days, a sufficient period to obtain at least $6 \times$ global coverage of the lunar surface (every ≈ 14 days), without loss of direct measurements over the lunar farside. The mission's measurement approach was modeled after that of the highly successful Gravity Recovery And Climate Experiment (GRACE) mission¹, and used a Ka-band Lunar Gravity Ranging System (LGRS) payload derived from that on GRACE to obtain highly precise (measurement noise $< 10^{-9}$ km/s) inter-spacecraft range-rate measurements, synchronized using the inter-spacecraft S-band link of the Time Transfer System (TTS). Additionally, Ultra Stable Oscillators (USOs) on each spacecraft allowed for X-band one-way Doppler tracking with Earth, backed up by S-band two-way Doppler tracking with Earth, during un-occulted periods.

A fairly comprehensive discussion of the approach and estimation technique used in processing all of these data is presented in Ref. 2. Simulations of the gravity field recovery processing presented therein, performed prior to the primary science mission and any real data collection, demonstrated sufficient anticipated capability for achieving baseline mission success. The real data processing to date has already exceeded this anticipated performance threshold.^{3,4} However, we do not report in this paper any results from that ongoing processing, other than evaluation metrics for various approaches taken with the main focus herein: the particular portion of the methodology involving thermo-optical modeling of the two GRAIL spacecraft.

The broad science objectives for the GRAIL mission are to estimate the gravity field in order to determine the Moon's interior structure from crust to core, and better understand its thermal evolution. Six specific science investigations flow from this (see Ref. 5, pg. 3). Meeting the requirements associated with the first four investigations constitutes minimum mission success, and meeting the requirements associated with all six investigations constitutes baseline mission success. Prior to launch, to assess our ability to meet all of these requirements, we examined the effects of all known dynamic and kinematic error sources on the uncertainty of simulated solutions for the gravity field and for tidal parameters (k_2) and "core parameters" ($\Delta \bar{C}_{21}, \Delta \bar{S}_{21}$) characterizing the time-varying signature of a possible solid inner core. Early calculations of the relative magnitude of these effects revealed that the non-gravitational acceleration in reaction to spacecraft thermal re-radiation was among the dominating sources of simulated solution uncertainty. This was particularly true

for the long-wavelength component of the gravity field and for the core parameters that are most pertinent to satisfying the requirements of investigations five and six.

This motivated developing detailed thermal and optical models of the spacecrafts and using them with appropriate data to accurately calculate the thermal re-radiation acceleration (as well as SRP acceleration) included in the vector summation of perturbing accelerations on each spacecraft in the dynamical model. This dynamical model is incorporated within JPL’s Multiple Interferometric Ranging And GPS Ensemble (MIRAGE) software set, used to perform both the orbit determination steps in level 1 data processing (conversion of raw dual one-way inter-spacecraft range to instantaneous range-rate measurements) and the entirety of level 2 data processing (actual gravity field estimation).

In this paper, we first describe the thermo-optical models, then their use with temperature vs. time profiles from pre-launch finite-element-based thermal simulations. We describe how parameter sensitivity studies using such profiles led to the choice of nominal and off-nominal acceleration cases bounding uncertainties. We describe derivation, from the difference of these cases, of an apriori error model for parameters estimated to soak up otherwise unmodeled accelerations. We then describe our shift from interpolation of calculated accelerations to interpolation of temperatures, to get pre-launch thermal simulation derived (PTSD) surface and sensor location temperatures, concurrent with temperature sensor telemetry. We describe the translation of the latter into temperature telemetry derived (TTD) surface temperatures. We present options for the nominal acceleration history and corresponding apriori error model to be passed into MIRAGE for the gravity field recovery. We conclude with recommendations for the apparent best methodology to use.

II. Thermo-Optical Models

Prior to fall 2010, different models for the GRAIL spacecrafts relevant to the calculation of radiation-based non-gravitational accelerations were being used by different people or groups working on the GRAIL project. These included the Lockheed Martin Astronautics ACS team (primarily with an interest in solar radiation torque), the JPL navigation team (for navigation simulations), the gravity science team (for MIRAGE simulations of the gravity analysis process), and the first author of this paper (for the preliminary thermal re-radiation acceleration sizing calculations motivating this effort). The inconsistency was brought up as a potential concern in a project meeting, after which a set of new models was created from the best available information.

These models have varying levels of detail but are all reconciled with each other in the sense of having geometric and optical parameters such that they should all provide roughly equivalent computations of the non-gravitational accelerations on the spacecrafts due to radiation. This includes both incoming radiation, as for the SRP or Lunar albedo pressure or Lunar thermal emission pressure, and outgoing radiation, as for the thermal re-radiation acceleration.

The most detailed model in this set contains 28 single-sided plate surfaces for each of GRAIL-A and GRAIL-B, covering most of their exteriors. Small details and protuberances such as the thrusters and MoonKAMs (the education and public outreach secondary payload) were not captured in this. The two spacecraft are nearly identical but externally mirrored about the $X - Z$ plane of the mechanical reference frame (hereafter, simply “body-frame”). This was by design, since during the primary science mission, pointing of the LGRS antennae towards each other required that GRAIL-B (leading in orbit) have its $+Y$ axis toward nadir, and GRAIL-A (trailing in orbit) have its $-Y$ axis toward nadir. With Lunar albedo and Lunar thermal emission loading from the nadir-facing side, the two spacecraft were given different surface material treatments in their $\pm Y$ directions, which was accurately captured. The definition of surfaces in this highest fidelity model, including surface materials, directions of outward surface normals $\hat{\mathbf{n}}_i$ in the body frame, and areas A_i , is given in Table 1. These surfaces are illustrated for GRAIL-B in Fig. 1 with the boxed numbers matching the number in the first column of Table 1. GRAIL-A would appear similar except for the differences tabulated.

We combined surfaces in the most detailed model to create three successively lower plate-count models of the spacecrafts. Combination of surfaces was done first for common material and orientation, then for just common orientation. Combination was performed in a way to keep the models equivalent in four quantities: power coming into each spacecraft, acceleration on each spacecraft due to SRP, power coming out of each spacecraft, and acceleration on each spacecraft due to thermal re-radiation. The result of combination for common material and orientation was a model containing 17 single-sided plate surfaces for each of GRAIL-A and GRAIL-B.

Table 1. Surface definition for highest fidelity spacecraft thermo-optical model

#	Description of surface	Direction of \hat{n}_i		A_i (m ²)		Surface Material	
		GR-A	GR-B	GR-A	GR-B	GR-A	GR-B
1	+X bus panel	+X	+X	0.58361		MLI*	
2	GPA radiator	+X	+X	0.03071		Silver Teflon	
3	USO radiator	+X	+X	0.017032		Silver Teflon	
4	RSB radiator	+X	+X	0.0069677		Silver Teflon	
5	−X bus panel	−X	−X	0.47691		MLI*	
6	Launch vehicle adaptor ring	−X	−X	0.16141		Aluminum Foil	
7	+Y bus panel	+Y	+Y	0.64756	1.025	MLI*	
8	+Y panel +Z radiator extension	−Y	−Y	0.094747		MLI*	Z-93C55
9	+Y panel −Z radiator extension	−Y	−Y	0.069481		MLI*	Z-93C55
10	−Y bus panel	−Y	−Y	0.99971	0.62229	MLI*	
11	MRO-light radiator	+Y	−Y	0.37742		White Paint Z-93C55	
12	−Y panel, +Z radiator extension	+Y	+Y	0.069481		Z-93C55	MLI*
13	−Y panel, −Z radiator extension	+Y	+Y	0.069481		Z-93C55	MLI*
14	+Z bus panel	+Z	+Z	0.45064		MLI*	
15	Battery radiator	+Z	+Z	0.022581		Silver Teflon	
16	Warm gas generator radiator	+Z	+Z	0.10081		Beta-Alumina Coating	
17	Star tracker radiator	+Z [†]	+Z [†]	0.1089		White Paint Z-93C55	
18	−Z bus panel	−Z	−Z	0.4719		MLI*	
19	MIMU radiator	−Z	−Z	0.15903		White Paint Z-93C55	
20	MWA radiator	−Z	−Z	0.052		Silver Teflon	
21	+Y solar array, front	−X	−X	1.9366		Solar Cells	
22	+Y solar array, back	+X	+X	1.9366		Bare M55J	
23	−Y solar array, front	−X	−X	1.9366		Solar Cells	
24	−Y solar array, back	+X	+X	1.9366		Bare M55J	
25	−X panel, +Z array closeout, front	−X	−X	0.47391		White Paint Z-93C55	
26	−X panel, +Z array closeout, back	+X	+X	0.47391		MLI*	
27	−X panel, −Z array closeout, front	−X	−X	0.47391		White Paint Z-93C55	
28	−X panel, −Z array closeout, back	+X	+X	0.47391		MLI*	

* Aluminized Kapton, and from previous data, the Kapton side is assumed to face outward.

† Approximately, ignoring cant in anti-nadir direction.

The result of doing combination for just common orientation was a model containing 8 single-sided plate surfaces for each of GRAIL-A and GRAIL-B, one for each of the principal axis directions (−X,+X,−Y,+Y,−Z,+Z) to represent the bus and its wings/extension, one for the combined solar array cell sides, and one for the combined solar array back sides. In addition another ‘bus’ component was included to model residual SRP with the estimated ‘soak-up’ parameters G_X and G_Y .

Finally, a coarsest model was created, containing 5 plate surfaces for each of GRAIL-A and GRAIL-B, three of them ‘bidirectional’ and two of them single-sided, plus a ‘bus’ component to model residual SRP with the estimated ‘soak-up’ parameters G_X and G_Y . What is meant by a bidirectional surface is a double-sided plate with no difference between the front and the back. Only the projected area of the plate on the plane normal to the direction to the sun, the smaller of the two angles of the two opposing plate surface normal vectors away from the direction to the sun, and the plate optical properties (assumed the same between front and back) are used for the SRP calculation. Two distinct directional (i.e. the usual single-sided) surfaces are defined for the combined solar array cell sides and combined solar array back sides.

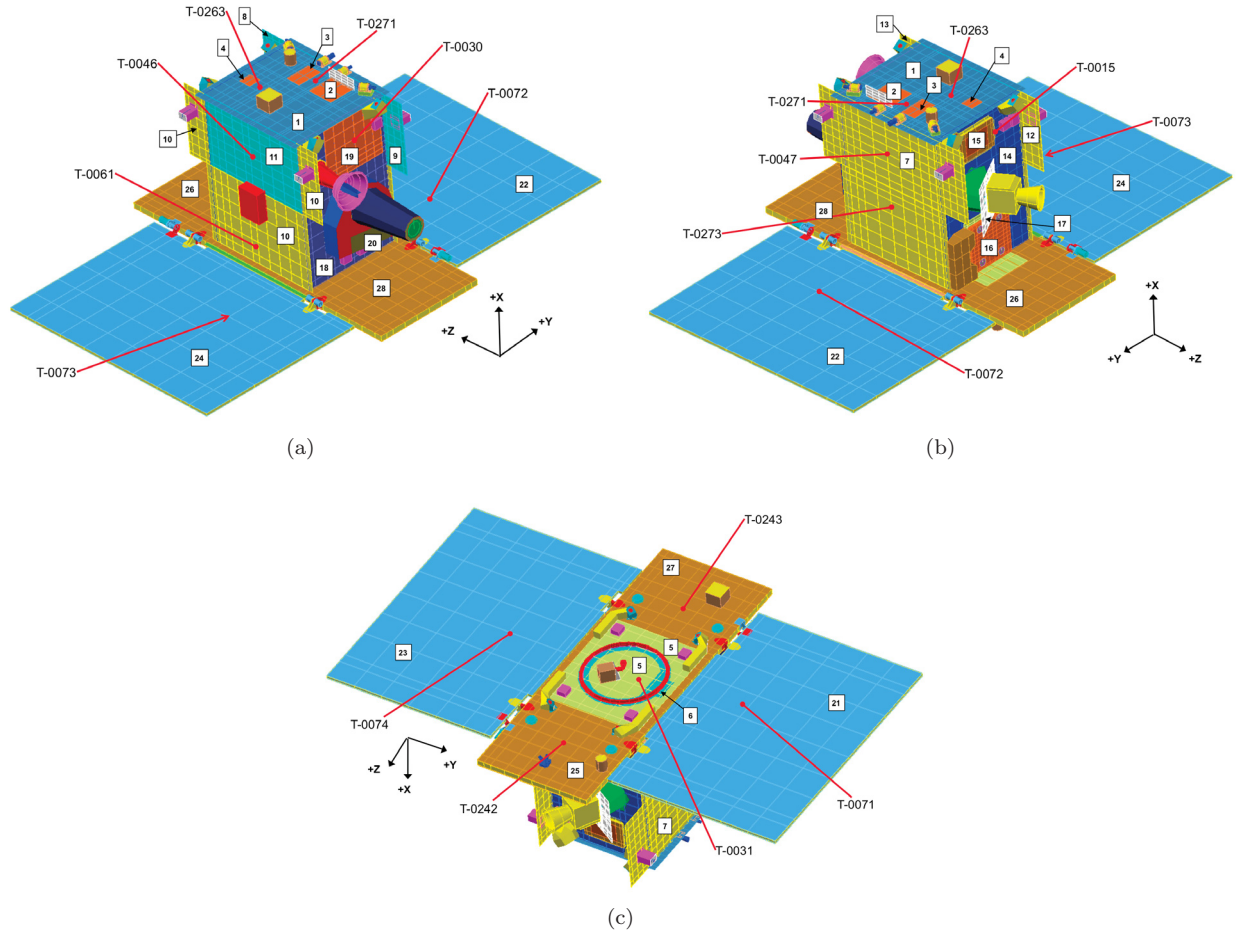


Figure 1. Placement of surfaces on GRAIL-B in highest fidelity model.

The mapping for combination of surfaces to obtain the successively smaller models is shown in Fig. 2 and Fig. 3 for GRAIL-A and for GRAIL-B, respectively. We desired that the combination of surfaces preserve the same value between the different models for each of the four quantities calculated with the following expressions:

$$P_{in} = \frac{C_1 c p(t)}{r_p^2} \sum_i A_i \alpha_i \cos \psi_i(t), \quad (1)$$

$$\mathbf{a}_{srp} = \frac{C_1 p(t)}{m_{S/C} r_p^2} \sum_i \left\{ -\hat{\mathbf{n}}_i A_i (2 \nu_i \cos \psi_i(t) + 4 \mu_i \cos^2 \psi_i(t)) + \hat{\mathbf{r}}(t) A_i (1 - 2\mu_i) \cos \psi_i(t) \right\}, \quad (2)$$

$$P_{out} = \sigma_{SB} \sum_i \left\{ A_i \epsilon_i (T_i(t) + \Delta T_i(t))^4 \right\}, \quad (3)$$

$$\mathbf{a}_{therm} = \frac{2}{3} \frac{\sigma_{SB}}{m_{S/C} c} \sum_i \left\{ -\hat{\mathbf{n}}_i A_i \epsilon_i (T_i(t) + \Delta T_i(t))^4 \right\}. \quad (4)$$

The legacy Orbit Determination Program (ODP) specular reflectivity parameter and diffuse reflectivity parameter, appearing in Eq. 2 above and used within MIRAGE, are related to the actual specular reflectivity C_{s_i} and actual diffuse reflectivity C_{d_i} , for which $\alpha_i + C_{s_i} + C_{d_i} = 1$, as follows:

$$\mu_i = \frac{1}{2} C_{s_i} \quad , \quad \nu_i = \frac{1}{3} (C_{d_i} + \alpha_i \epsilon_i). \quad (5)$$

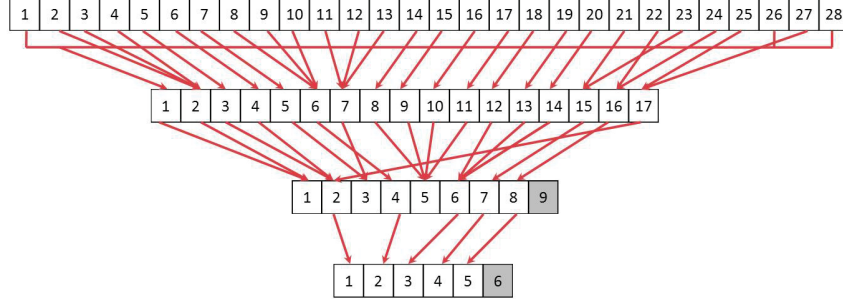


Figure 2. Relationships for combination of surfaces from one model to the next, for GRAIL-A.

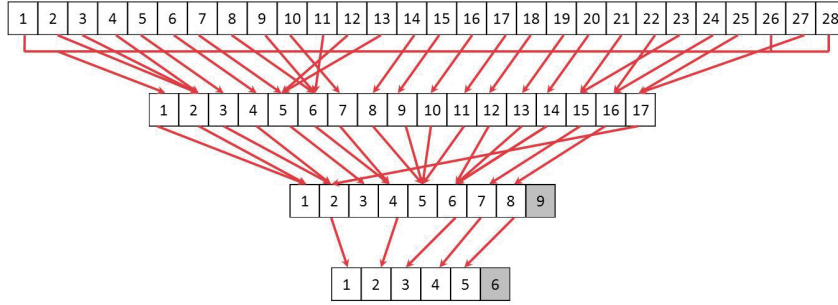


Figure 3. Relationships for combination of surfaces from one model to the next, for GRAIL-B.

Note that the while the outward surface normal $\hat{\mathbf{n}}_i$ of each surface is time-invariant in the spacecraft body-fixed frame, the unit direction vector from the sun to the spacecraft $\hat{\mathbf{r}}$ is time-varying in that frame. Accompanying this, each surface has a time-dependent solar incidence angle $\psi_i(t)$, and a time-dependent spatially averaged (over the surface) temperature $T_i(t)$, plus any temperature bias applied $\Delta T_i(t)$. Suppose that n surfaces, all with normals in the same direction but not necessarily of the same material, are being combined into one new surface. The area of the new surface is just $\bar{A} = \sum_{i=1}^n A_i$. Denoting other properties of the combined surface with an overbar too, we want to set $\mathbf{a}_{therm}(n \text{ surfaces}) = \mathbf{a}_{therm}(\text{new surface})$. Assuming that the temperature profile of the largest (in area) surface among those being combined to form the new surface is also applied to the new surface for purposes of computing a thermal re-radiation acceleration due to the new surface, we find the new surface's time-varying effective emissivity as follows:

$$\bar{\epsilon}(t) = \left(\sum_{i=1}^n \{A_i \epsilon_i (T_i(t) + \Delta T_i(t))^4\} \right) (\bar{A} (\bar{T}(t) + \Delta \bar{T}(t))^4)^{-1}.$$

Setting $P_{out}(n \text{ surfaces}) = P_{out}(\text{new surface})$ gives the same relationship. Note that depending on how the area of the largest surface being combined and the area of the new surface compare, and on how the temperature profile for that largest surface and the other surfaces being combined compare, this expression can produce an *effective* emissivity for the new combined surface higher than unity, i.e. higher than for a blackbody perfect emitter. We take the average over all time for a new value for the emissivity of the new combined surface in the next smaller model. Setting $\mathbf{a}_{srp}(n \text{ surfaces}) = \mathbf{a}_{srp}(\text{new surface})$ or $P_{in}(n \text{ surfaces}) = P_{in}(\text{new surface})$ also gives the relationships:

$$\bar{\mu} = (\bar{A})^{-1} \sum_{i=1}^n (A_i \mu_i) \quad , \quad \bar{\nu} = (\bar{A})^{-1} \sum_{i=1}^n (A_i \nu_i) \quad , \quad \bar{\alpha} = (\bar{A})^{-1} \sum_{i=1}^n (A_i \alpha_i). \quad (6)$$

For the highest fidelity model, before this combination process, we used the best available material optical properties for each surface material called out in Table 1. The values used are summarized in Table 2. The beginning of life (BOL) and end of life (EOL) values given should roughly bracket the time variation of the material properties due to ongoing degradation of the materials from their post-bake-out condition at the time of launch. Actual material properties used in the calculation of body-frame srp and thermal acceleration vectors via Eqs. 2 and 4 were computed using a linearly weighted average employing the ratio χ of the duration from the actual date of launch to the epoch of calculation (numerator) over one year (denominator). This was done because several of the EOL values were obtained from measured BOL values using one year on geosynchronous Earth orbit environment degradation curves found in a Lockheed Martin spacecraft thermal engineering standard (which should be very conservative for the lunar environment). As χ goes from 0 to 1, α_i goes from the minimum of BOL and EOL values to the maximum of BOL and EOL values (since absorptivity tends to increase with degradation), while ϵ_i and C_{s_i} go from the maximum of BOL and EOL values to the minimum of BOL and EOL values (since emissivity and specular reflectivity tend to decrease with degradation).

Table 2. Optical properties definition for surface materials in highest fidelity model

Material Name	BOL Properties				EOL Properties			
	α	ϵ	C_s	C_d	α	ϵ	C_s	C_d
MLI (Aluminized Kapton)*†	0.41	0.72	0.55	0.04	0.47	0.72	0.49	0.04
Silver Teflon*†	0.09	0.78	0.85	0.06	0.14	0.78	0.80	0.06
White Paint Z-93C55*†	0.16	0.91	0.04	0.80	0.21	0.91	0.04	0.75
Solar Cells*	0.91	0.84	0.09	0	0.91	0.84	0.09	0
Bare M55J*	0.92	0.70	0	0.08	0.92	0.70	0	0.08
Warm Gas Radiator*†	0.25	0.89	0.04	0.71	0.30	0.89	0.035	0.07
Aluminum Foil*	0.18	0.01	0.66	0.16	0.18	0.01	0.66	0.16

* BOL properties measured after exposure to 24 hr of 125°C vacuum bakeout.

† EOL properties degraded from BOL properties as in text.

All of the above models were compiled into ASCII (plain text) input files, formatted for JPL’s Mission-analysis, Operations, and Navigation Toolkit Environment (MONTE) software system, and also formatted for MIRAGE. The simplest model was used internally within MIRAGE for calculation of the SRP acceleration, and optionally the Lunar albedo pressure and Lunar thermal emission pressure accelerations as well. Note that for MIRAGE to correctly use any such plate surfaces model, an external program must be run first that computes illumination of the surfaces with raytracing from the source appropriate to the acceleration under consideration, accounting for self-shadowing of surfaces. This program then computes each surface’s projected illuminated area on the plane normal to the source direction, and outputs an area scale factor on that surface/component read in during the MIRAGE run. If attempting to use one of the more detailed models with more single-sided surfaces, this self-shadowing program would need to be modified to not only get the projected illuminated area but resolve whether each $\hat{\mathbf{n}}_i$ is more than 90° away from the source direction, and if so, zero the projected illuminated area. The effort for this modification was not viewed as justified, so the more detailed models have not yet been used for calculation of the accelerations due to these causes.

The most detailed model, however, was used to calculate thermal re-radiation acceleration per Eq. 4. Finite-element-based thermal simulations using Thermal Desktop® (a GUI for SINDA/FLUINT) were performed by the spacecraft thermal team for each spacecraft for the thermal loading conditions of several β angles during the primary science mission. The thermal loading included incident sunlight, incident lunar albedo / infrared emission, operation of all spacecraft equipment per planned modes, etc. After reaching a “steady-state” (i.e. nearly repeating in time-varying profile from orbit to orbit), nodal output of these simulations over one orbit period was spatially averaged over the plate surfaces to produce average surface temperature vs. time profiles $T_i(t)$ over one orbit. At the same time stamps, node temperatures nearest the locations where relevant temperature sensors were placed on each spacecraft (outwardly visible locations shown for GRAIL-B with T-0XXX markers in Fig. 1) were picked out from the results to produce simulated sensor temperature vs. time profiles $T_j(t)$ over the same orbit. All this was done for a “worst-case hot”

scenario and a “worst-case cold” scenario, employing respectively the optical properties and thermal loading to produce the maximum and minimum expected temperatures during spacecraft operations, and for each of $\beta = 49^\circ, 77^\circ, 83^\circ, 90^\circ$. While the spacecraft thermal team was interested in examining these extremal temperatures to assure they fit within material and equipment requirements, the actual current best estimate temperature profiles were desired for our purposes. Material degradation tends to move the spacecraft temperatures from the “worst-case cold” conditions toward the “worst-case hot” conditions with the passage of time, so for each β we employed skew-averaging between the “worst-case cold” and “worst-case hot” conditions by the χ matching the epoch at which that β is achieved. Note this χ differs between the same β case before and after the maximum β near the midpoint of the primary science mission. The resulting “averaged” case temperature vs. time profiles were used with Eq. 4, producing the results shown for each body-frame component in Fig. 4.

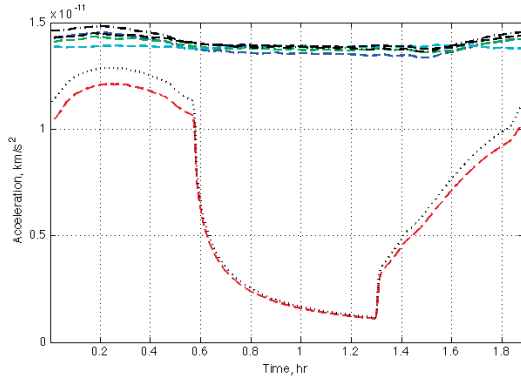
III. Sensitivity Studies and Apriori Error Model

We sought to determine the sensitivity of the thermal re-radiation acceleration profiles produced as in the last section, for the specific β ’s/epochs in Fig. 4, to various assumptions and parameter uncertainties in the thermo-optical model and to uncertainties in the input temperature profiles used with that model.

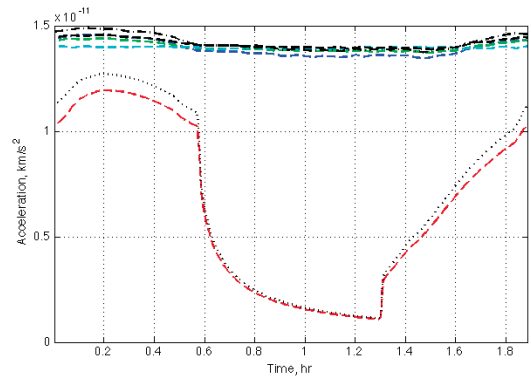
For example, for the solar array surfaces (the surfaces having the largest contribution to thermal re-radiation acceleration) we quantified the difference that assuming spatial averaging had made vs. no such spatial averaging. This was done by producing a temperature contour plot on each panel face from the nodal output of one of the FE-based thermal simulations, letting the areas between contours be at the temperatures midway between that of the contours, applying the same equation with a more finely divided sum over areas, and then differencing the result from that using surface-averaged temperature. For the +Y panel, the Δ in acceleration on the cell side was +0.29%, the Δ on the back side was −0.47%, and the Δ in the net acceleration contributed by the panel was +2.16%. This implied no significant loss of fidelity in performing the spatial averaging over surfaces.

Similarly, we quantified sensitivity to extracting power from the arrays by running a simulation case with all power left on the arrays and a case with all power extracted from them (bounding the effects of solar cell string switching under different power modes). We also calculated the effects of 3σ variations in optical properties of every material in use and shown in Table 2. And we calculated the response to constant additive worst-case temperature biases ΔT_i on all surfaces, made in the sense of always pushing the spacecraft in one direction on each body axis. For example, for pushing toward +X, we biased the average temperature of surfaces with $\hat{\mathbf{n}}_i$ toward −X by a positive constant and biased the average temperature of surfaces with $\hat{\mathbf{n}}_i$ toward +X by the negative of that constant. A 5 K global bias in this sense seemed to bound most changes resulting from all the realistic input variations explored (See Fig. 5). Thus the difference in calculated thermal re-radiation acceleration between that 5 K bias off-nominal case and the nominal case was taken as indicative of the magnitude of unmodeled accelerations that would act on each spacecraft, on top of the nominal thermal re-radiation acceleration and all other nominal accelerations applied.

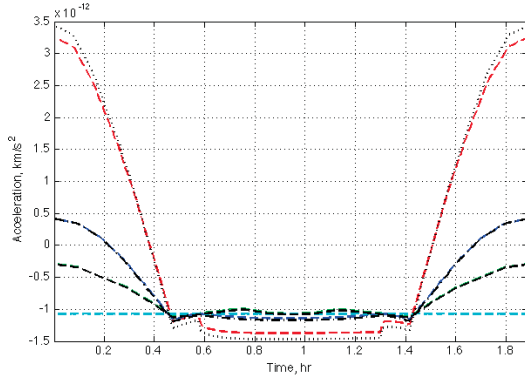
The thermal re-radiation acceleration profiles over one orbit at the seven specific β -epochs were linearly double-interpolated over phase angle ϕ in the orbit (analogous to sub-latitude, capturing the fast variation within the curve) and β (capturing the slow variation of the curve itself), for the (ϕ, β) values calculated from the trajectory at any epoch in the primary science mission. This produced nominal and 5 K bias thermal re-radiation acceleration histories for the whole primary science mission. The difference between these was used to create an apriori error model for the periodic acceleration parameters estimated to absorb all unmodeled accelerations during the level 1 and level 2 science data processing. These periodic acceleration parameters were estimated for every orbital period (nominally ≈ 6813 seconds) spaced within each data arc (typically a few days in length). The scheme used was to place close-fitting upper and lower bound curves around the plot of each component of $\mathbf{a}_{therm,5K} - \mathbf{a}_{therm,nom}$ translated into the instantaneous radial-tangential-normal (RTN) frame of the spacecraft in question. Then the constant periodic acceleration parameter apriori σ ’s were set equal to the maximum absolute value of these bounding curves, and the once/rev and twice/rev sinusoidal periodic acceleration parameter apriori σ ’s were set equal to the absolute value of the difference of these bounding curves. Pre-flight simulations of the data processing approach indicated this scheme would yield improved performance in the recovery of the long-wavelength gravity field and core parameters.



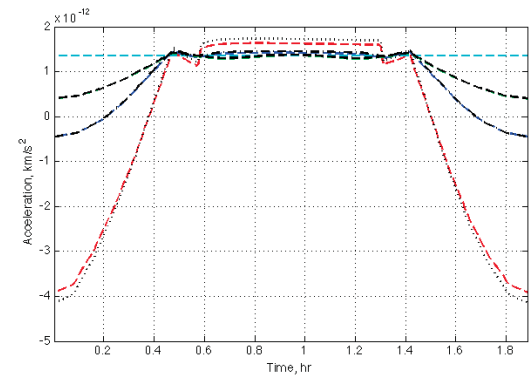
(a) GRAIL-A body frame X axis



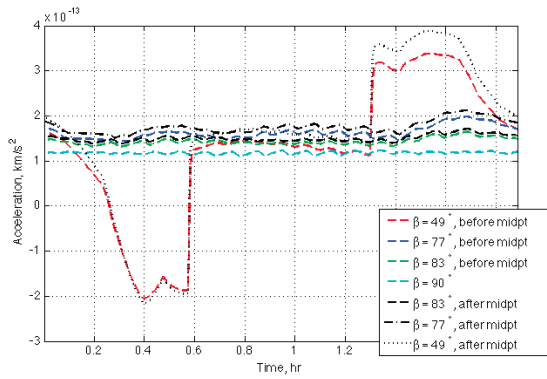
(b) GRAIL-B body frame X axis



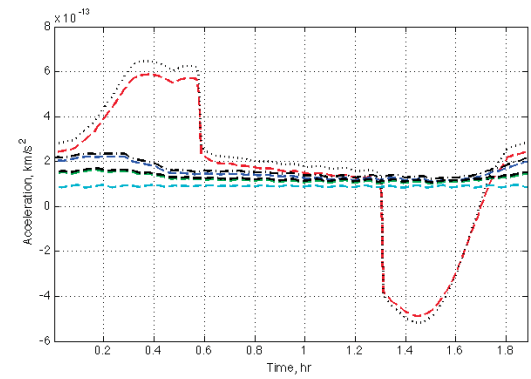
(c) GRAIL-A body frame Y axis



(d) GRAIL-B body frame Y axis

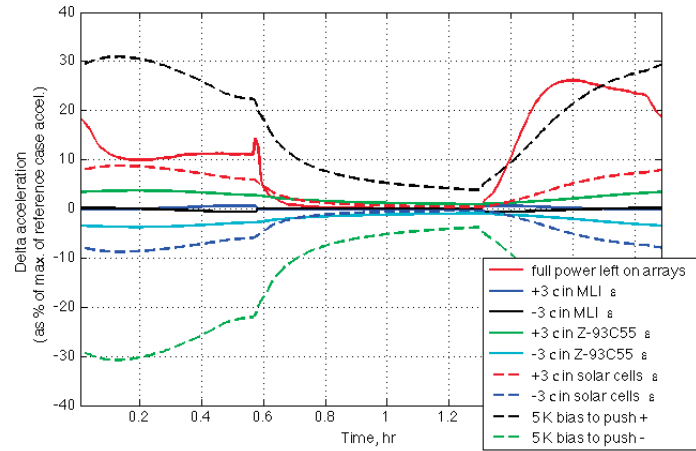


(e) GRAIL-A body frame Z axis

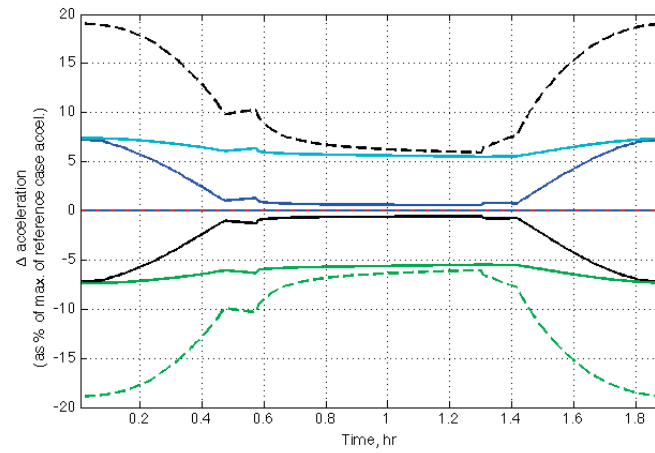


(f) GRAIL-B body frame Z axis

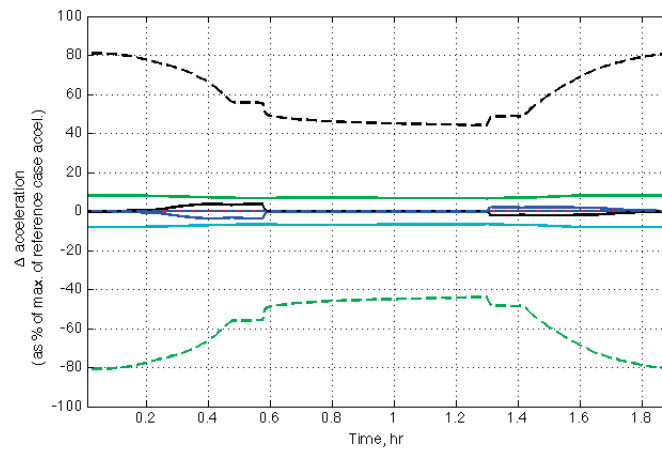
Figure 4. Acceleration profiles at specific β angles before and after the approximate midpoint of the primary science mission. The same legend applies to all panels.



(a) GRAIL-A body frame X axis



(b) GRAIL-A body frame Y axis



(c) GRAIL-A body frame Z axis

Figure 5. Sensitivity of acceleration profiles for one of the two spacecrafts to various deviations in model inputs away from the reference case, all shown for $\beta = 49^\circ$. The same legend applies to all panels.

IV. Leveraging Spacecraft Telemetry

We sought to utilize engineering housekeeping information downlinked from the spacecrafts during the primary science mission to improve the quality of our calculated nominal thermal re-radiation acceleration history and matching apriori error model used in processing the real data. With this in mind, we shifted from double-interpolation of calculated accelerations at (ϕ, β) of epoch to double-interpolation of temperatures at (ϕ, β) of epoch. This gave pre-launch thermal simulation derived (hereafter PTSD) surface and sensor location temperatures at any time stamp t of the telemetry data of interest. As for that, the thermistor channels used are listed in Table 3, and again, the outwardly visible ones among these thermistors have their locations indicated in Fig. 1. Readings on these channels were available every 20 seconds, on average.

Table 3. On-spacecraft temperature sensor channels of interest, same for both GRAIL-A and GRAIL-B

Label	Description	Surface Assoc.
T-0040	USO Temp 1	3
T-0056	USO Temp 2	3
T-0262	USO Temp 3	3
T-0272	USO Temp 4	3
T-0009	GPA Temp 1	2
T-0025	GPA Temp 2	2
T-0255	CDH Baseplate Temp	
T-0253	MIMU Temp	18, 19, 20
T-0012	MoonKam DVC Temp 1	
T-0028	MoonKam DVC Temp 2	
T-0073	Solar Array $-Y$ Temp 1	24
T-0074	Solar Array $-Y$ Temp 2	23
T-0071	Solar Array $+Y$ Temp 1	21
T-0072	Solar Array $+Y$ Temp 2	22
T-0243	$-X -Z$ Panel Ext Temp	27, 28
T-0031	$-X$ Panel Temp	5, 6
T-0242	$-X +Z$ Panel Ext Temp	25, 26
T-0046	$-Y$ Panel Temp 1	10, 12, 13
T-0061	$-Y$ Panel Temp 2	10
T-0030	$-Z$ Panel Temp	18, 19, 20
T-0263	$+X$ Panel Temp 1	1, 4
T-0271	$+X$ Panel Temp 2	1
T-0047	$+Y$ Panel Temp 1	7, 8, 9, 11
T-0273	$+Y$ Panel Temp 2	7
T-0015	$+Z$ Panel Temp	14, 15, 16
T-0244	TTS Antenna Bracket Temp	
T-0008	Star Tracker Temp 1	17
T-0024	Star Tracker Temp 2	17
T-0051	Transponder Ext Temp	11

We desired to derive and use some sort of mapping from the values on these telemetry channels into temperature telemetry derived (hereafter TTD) average surface temperatures. Either the PTSD or TTD surface temperature histories could then be used to compute the nominal thermal re-radiation acceleration history, and get the apriori error model to match, via the earlier-detailed thermo-optical model and methodology.

Developing this mapping turned out to be nontrivial. We first attempted to represent it as a time-invariant matrix A_{ij} mapping from sensors to surfaces at any time t , one such matrix for each GRAIL data

processing arc in the science mission, considered separately. We intended to derive these matrices pre-flight, for the anticipated division of data arcs, by using PTSD values for $T_i(t)$ and $T_j(t)$ covering those anticipated arcs at the planned average 0.05 Hz sample rate. We attempted to employ a simple least-squares algorithm to refine an initial guess for the values of elements in each row \mathbf{A}_i of each \mathbf{A}_{ij} to minimize the cost function

$$J_i = \left(\frac{1}{N} \mathbf{z}_i^T \mathbf{z}_i \right)^{\frac{1}{2}}, \quad \mathbf{z}_i = \mathbf{T}_i - [\mathbf{T}_1, \dots, \mathbf{T}_j, \dots, \mathbf{T}_{29}] \mathbf{A}_i^T, \quad \mathbf{T}_i = [T_i(t_1), \dots, T_i(t_N)]^T. \quad (7)$$

This did not work well because the shapes of the temperature profiles within each orbit period throughout the arc were qualitatively different between the $T_i(t)$ and $T_j(t)$ (with a few exceptions such as the solar arrays), even for thermistors j located in close physical proximity to surface i . Several of the temperature sensors were mounted on the baseplates of heat-producing electronics hardware on the interior side of body panels whose exterior surface temperature is of interest, and the thermal profile changed considerably through the intervening layers. Even if the shapes of the curves were similar and well-correlated, this method proved rather tedious to try to use for each arc, arc-by-arc, because the arcs were being redefined on the fly during data processing after the primary science mission started, to fit between ACS reaction wheel momentum dumps, payload software reboots triggered, etc.

Thus we resorted to a linear combination scheme developed and applied during the earlier cruise phase of the mission when a very different (i.e simpler) thermal environment was experienced by each spacecraft (then in sun-pointing attitude mode and more distant from any planetary body). Given n total surfaces in the spacecraft model, each of the instantaneous surface temperatures $T_i(t)$, $i \in \{1, \dots, m\}$, $m < n$, was set equal to the average of one or more $T_j(t)$, associated with that surface according to the geometry. This is similar to the initial guess for the mapping matrix above. Each of the $n - m$ remaining surface temperatures is set equal to the likewise best associated one of the m surface temperatures, plus a bias ΔT . All these associations are indicated in Table 3.

There were two approaches exercised for this biasing. First, we found ΔT as the time average, over one orbit at the $\beta \approx 90^\circ$ epoch, of the PTSD temperature profile for each of the $n - m$ surfaces minus the PTSD temperature profile for the associated one of the m surfaces. The $\beta \approx 90^\circ$ epoch has the $-X$ body-frame axis pointing directly toward the sun, as during the cruise phase, which is why this approach was first used during the cruise phase. This approach was expected to become quite inaccurate at lower- β conditions (during the beginning and ending weeks of the primary science mission). So second, we found the bias necessary to match the time average over one day (≈ 12.7 orbit periods) of the PTSD temperature profile for the one of the $n - m$ surfaces with the last iteration of the TTD profile for the same surface. This was done for the day spanning each of the specific β 's/epochs in Fig. 4, and then another linear weighted-averaging with time was employed to obtain ΔT in between these epochs. This approach worked far better. With either approach the mapping from “raw” telemetry to arrive at the TTD surface temperature history itself became dependent on the PTSD surface temperature history (and with the latter one, iteratively dependent, but weakly so).

Applying the thermo-optical model after all of this and comparing the PTSD and TTD thermal re-radiation acceleration histories for the same times indicated considerable discrepancy, shown for an example period late in the primary science mission within Fig. 6. The spikes in the discrepancy (black curve) near the beginning and end of the downward “shark-fin” pattern in the profiles themselves (blue, red curves) are due to misalignment in the timing of transit into and out of the moon’s shadow between what the simulation predicts and what the telemetry measures. The simulations had been set up for a perfectly circular orbit with a slightly shorter orbital period than the actual orbit period (6785.51 vs. ≈ 6813 seconds) but, more importantly, they did not properly account for the changing eclipse duration up until eclipsing stopped at approximately 1 AM UTC on April 2, 2012 and after it resumed at approximately 1:30 PM UTC on May 4, 2012.

To fix this issue, we separately queried V_{oc} and I_{sc} telemetry channels sampled at the much higher rate of 1.05-1.07 Hz, and scanned through this telemetry data to more accurately determine the timestamps at which shadow entry/exit actually occurred. These quantities undergo a sharp change when the panels are shadowed vs. illuminated, so the algorithm used was simply to differentiate the V_{oc} (for example) signal, and flag when the maximum value of dV_{oc}/dt within a moving window of 20 successive data points was greater than a positive threshold value, if the last transition flagged was into shadow, or less than a negative threshold, if the last last transition flagged was coming into sunlight. A transition could only be flagged more than 90% of a nominal orbital period later than the last transition in the same direction. We employed

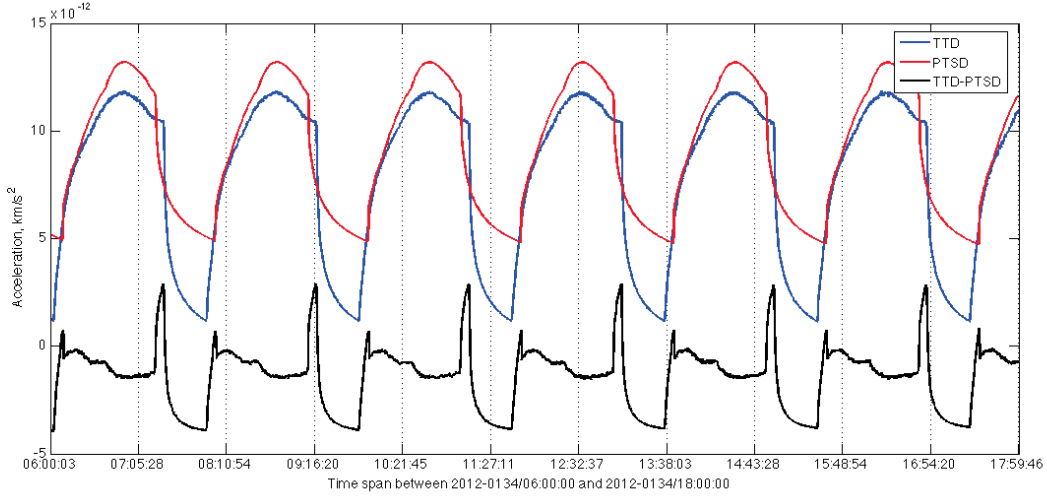


Figure 6. Comparison of net thermal re-radiation acceleration histories for GRAIL-A, body $\pm X$ axis, with linear β interpolation and no shadow entry/exit timing alignment behind the PTSD case.

a similar algorithm, with more complicated logic, to also scan and detect the transitions in the average of the two solar panel front faces' PTSD temperature histories. This gave two sets of shadow entry/exit timestamps, with a 1-to-1 correspondence between them. Let t_l and t_k be the timestamps of the same event from the V_{oc} and $T_{21,23}$ respectively. We shifted and stretched/compressed in time the PTSD temperature values for all $t \in [t_k, t_{k+1}]$ using $t' = t_l + (t_{l+1} - t_l)(t - t_k)/(t_{k+1} - t_k)$. The resulting comparison of thermal re-radiation acceleration histories on the same time period and vertical scale is shown in Fig. 7.

This still shows a large difference in that the the PTSD temperatures are far too warm during eclipse periods. In reality, the drop in these surface temperatures during eclipse remains at about the same depth as at the beginning of the primary science mission and just decreases in duration. The failure to capture this was traced to the double-interpolation of temperatures mentioned at the beginning of this section, particularly the improper linear interpolation with respect to β between the $\beta = 49^\circ$ and $\beta = 77^\circ$ profiles when epochs were outside the April 2 – May 4 period of no eclipsing. We replaced this with measuring the nearest (in time) eclipse duration from the V_{oc} shadow/entry exit times detected, and using the ratio of that over the maximum eclipse duration in the whole mission to nonlinearly interpolate between the $\beta = 49^\circ$

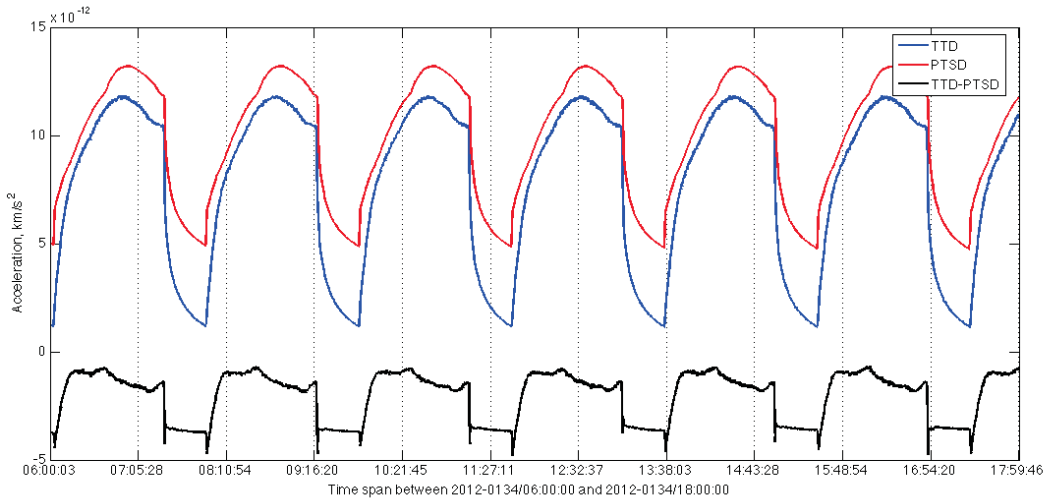


Figure 7. Comparison of net thermal re-radiation acceleration histories for GRAIL-A, body $\pm X$ axis, with linear β interpolation but with shadow entry/exit timing alignment behind the PTSD case.

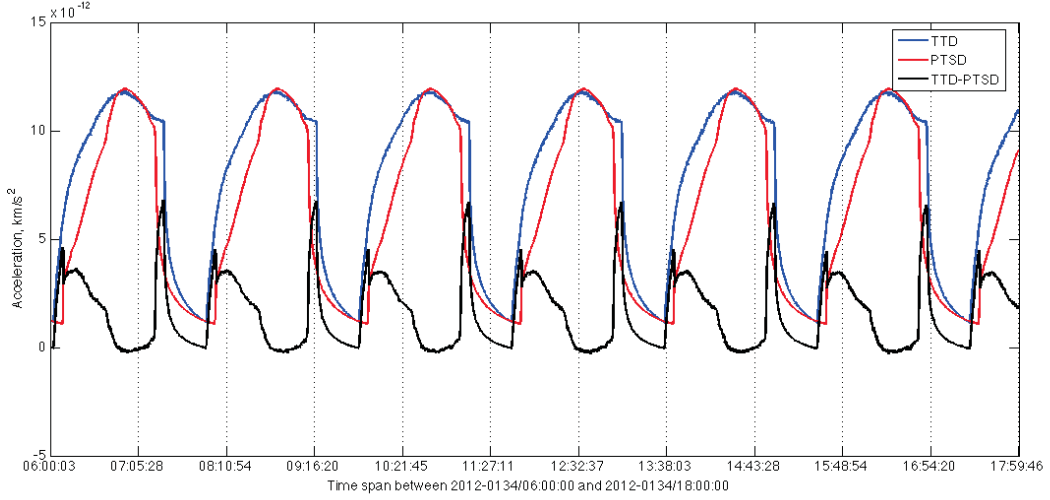


Figure 8. Comparison of net thermal re-radiation acceleration histories for GRAIL-A, body $\pm X$ axis, with interpolation according to eclipse duration ratio but no shadow entry/exit timing alignment behind the PTSD case.

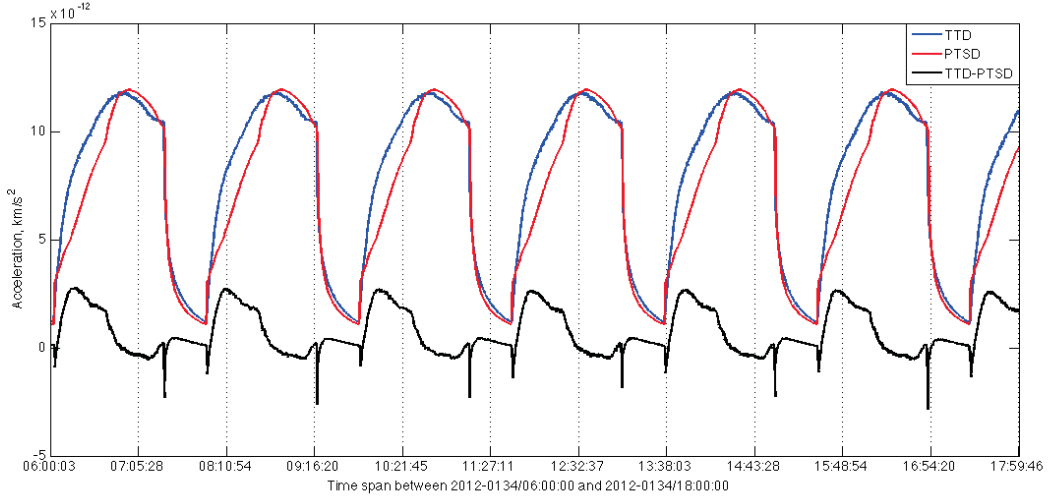


Figure 9. Comparison of net thermal re-radiation acceleration histories for GRAIL-A, body $\pm X$ axis, with interpolation according to eclipse duration ratio and with shadow entry/exit timing alignment behind the PTSD case.

and $\beta = 77^\circ$ profiles outside the above no-eclipsing period. The same thermal re-radiation acceleration history comparison after applying this change of interpolation method, and both before and after applying the alignment of shadow entry/exit timing, is shown in Figs. 8 and 9.

Once both corrections are applied, we see that the time-averaged level of the deviation between the TTD and PTSD acceleration histories is about 10% of the peak in those histories, for the $\pm X$ body-frame direction. The level of deviation is relatively worse in the $\pm Y$ and $\pm Z$ directions (on the order of several 10's of percent of the peak in the histories for those components). However, the $\pm X$ direction has by far the dominant effect, and we can have some confidence at this point that the TTD thermal re-radiation acceleration history is suitable to be used in MIRAGE processing.

V. Options for Science Data Processing

Here we present the options, to be passed into MIRAGE for the gravity field recovery, for the whole primary science mission's nominal thermal re-radiation acceleration history, and corresponding apriori error model. Recall that before deriving the apriori error model by the scheme described earlier at the end of

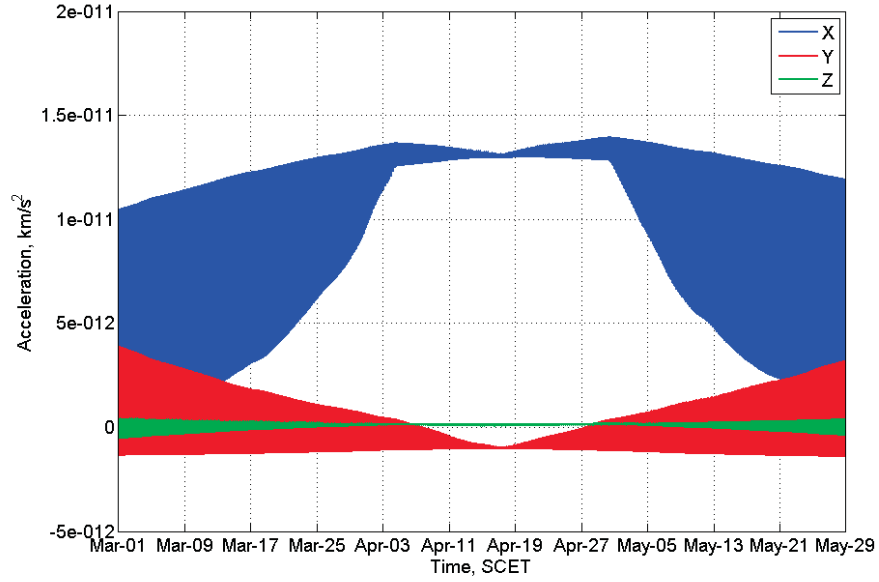


Figure 10. Nominal thermal re-radiation acceleration history for entire primary science mission for GRAIL-A, body frame components, for option of PTSD case and still using linear β interpolation but with shadow entry/exit timing alignment.

Section III, we also had to make a 5K off-nominal history relative to each nominal history. For this we biased TTD surface temperatures in just the same way we biased PTSD surface temperatures, so as to have all surfaces cause more net push in one direction. Once the apriori σ 's on all periodic acceleration parameters were calculated, we also enforced an overriding minimum value of 3×10^{-13} km/s² on those which came out smaller than that threshold. This was done because it was judged that the amplitude of the fast variation (i.e. variation within each orbit) of the acceleration *difference*, determining the gap between upper and lower bounding curves and hence the once- and twice-per-rev parameter apriori σ 's,

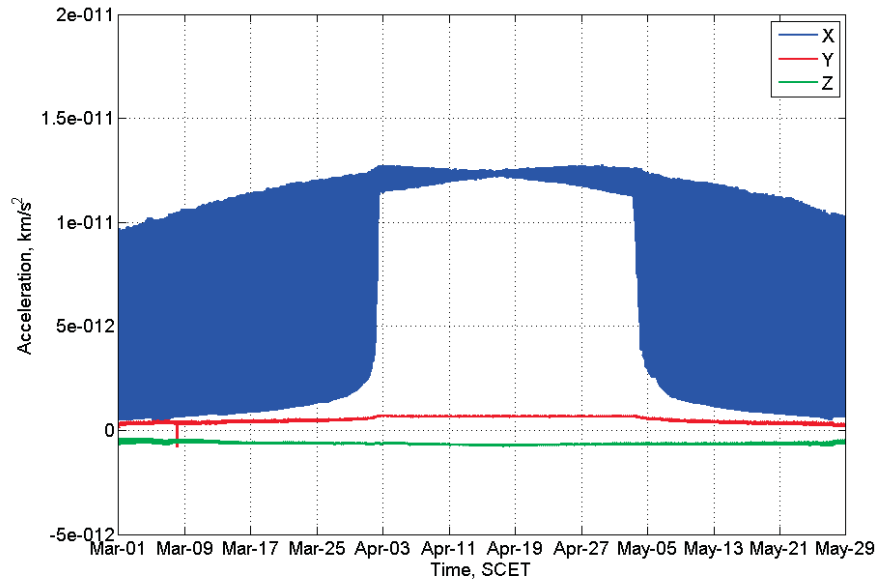
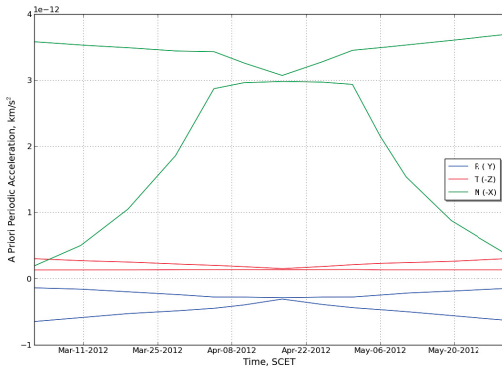


Figure 11. Nominal thermal re-radiation acceleration history for entire primary science mission for GRAIL-A, body frame components, for option of iterated TTD case.

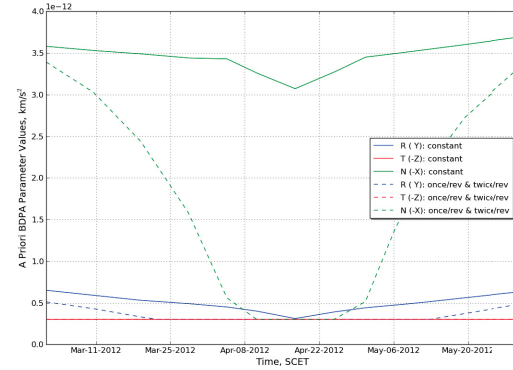
was sometimes too small relative to the likely “noise” in other unmodeled accelerations. The parameters initialized with such small uncertainty might be too tightly constrained to absorb those other unmodeled accelerations, allowing degradation of the gravity solution. This is all particularly applicable for the Y and Z body-frame components, and nearest the middle of the primary science mission.

What is expected to be the worst option for the nominal history is shown in Fig. 10. This is from the PTSD case and still using the erroneous linear β interpolation, although shadow entry/exit times are aligned (cf. red curve on Fig. 7). Note the fast variation within each orbit is too tightly packed to be visible when viewed over this long duration, resulting in solid bands. The corresponding bounding curves on the nominal vs. 5K off-nominal difference and final apriori uncertainties vs. time are plotted in Fig. 12.

Arguably a better option for the nominal history is shown in Fig. 11, from the iterated TTD case (cf. blue curve in Fig. 9). The corresponding bounding curves on the nominal vs. 5K off-nominal difference and final apriori uncertainties vs. time are plotted in Fig. 13. Several notable differences vs. before are apparent. First, on the X axis, notice the sharper “shoulders” approaching, from outside, the April 2nd through May 4th permanently sunlit period. The maximum magnitude reached in the X axis acceleration is also lower, but the better-matched PTSD cases would eliminate this difference (again, see Figs. 8 and 9).

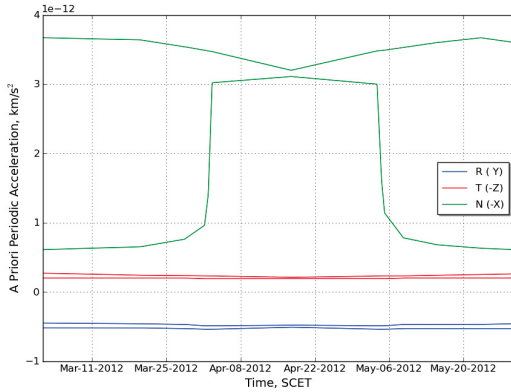


(a) Bounding curves on acceleration difference

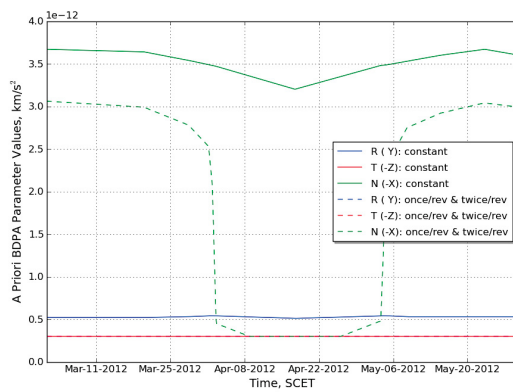


(b) Final apriori uncertainties, σ

Figure 12. A priori error model for GRAIL-A, in spacecraft instantaneous RTN frame, for option of PTSD case and still using linear β interpolation but with shadow entry/exit timing alignment.



(a) Bounding curves on acceleration difference



(b) Final apriori uncertainties, σ

Figure 13. A priori error model for GRAIL-A, in spacecraft instantaneous RTN frame, for option of iterated TTD case. Several of the curves are coincident, once the 3×10^{-13} km/s² minimum is put into effect.

Most importantly, on the Y and Z axes, the size of the fast variation of the acceleration itself (not difference of accelerations) is greatly reduced vs. before, while the bias level is also different in magnitude and sign. The latter fact is apparent from focusing on near the $\beta \approx 90^\circ$ epoch. The majority of the protuberances not captured within the plate geometry of our highest fidelity thermo-optical model (e.g.

TTS antenna bowl, star tracker optical inlet, etc.) are on the $+Z$ and $-Z$ faces, so the most area is missed on those faces. It is thus possible, though unlikely, that along the Z axis our modeling erroneously indicates far less thermal stability and a different net thermal balance than that achieved by the actual spacecrafts on orbit. But this does not explain the far larger discrepancy observed on the Y axis. A more likely explanation is that on these axes the fast variations are inappropriately damped out within the TTD acceleration profiles over each orbit, because the TTD surface temperature profiles are likewise inappropriately flattened. This is in turn because even the best sensors for mapping to the TTD surface temperatures for these axes are on equipment baseplates or the interior of body panels, and thus are being kept more thermally stable than the surfaces.

It would appear that perhaps the best option for science data processing is to use the most refined PTSD case, with eclipse duration ratio interpolation and with proper shadow entry/exit timing alignment, for the nominal history on the Y and Z body-frame axes, while using the iterated TTD case for the nominal history on the X axis, and deriving the apriori error model from this combined case.

VI. Conclusions

We have described in detail the development and application of thermo-optical models for GRAIL, especially for the goal of getting the best possible representation of the thermal re-radiation acceleration history. This has all been done with an eye toward reducing the tall pole in uncertainty of the overall budget of accelerations experienced by the twin spacecraft, other than that from the lunar gravity field being measured. This is to model the spacecraft dynamics accurately enough to improve both level 1 orbit determination and intermediate data product generation and level 2 gravity field solution generation, performed in iteration with each other to the point where all six science investigations' requirements are met. We have utilized a full time history of different kinds of spacecraft telemetry (temperatures, power characteristics) in this effort. But we have found that using this telemetry is of necessity coupled with using the results of thermal simulations performed pre-flight. The apparent best methodology to use in data processing from this point forward appears to be a hybrid thermal re-radiation acceleration history and apriori error model derived from both sensor telemetry and pre-flight simulations.

Acknowledgments

The work described in this paper was carried out at the Jet Propulsion Laboratory, California Institute of Technology, under a contract with the National Aeronautics and Space Administration. E. G. Fahnestock would like to thank the GRAIL Thermal, Operations, Navigation, and Science teams for their support in the execution of this effort.

References

- ¹Tapley, B. D., Bettadpur, S., Ries, J. C., Thompson, P. F., and Watkins, M. M., "GRACE Measurements of Mass Variability in the Earth System," *Science*, Vol. 305, 2004, pp. 503–505.
- ²Park, R. S., Asmar, S. W., Fahnestock, E. G., Konopliv, A. S., Lu, W., and Watkins, M. M., "Gravity Recovery and Interior Laboratory Simulations of Static and Temporal Gravity Field," *Journal of Spacecraft and Rockets*, Vol. 49, No. 2, 2012, pp. 390–400.
- ³Zuber, M. T., Smith, D. E., Asmar, S. W., Konopliv, A. S., Lemoine, F. G., Melosh, H. J., Neumann, G. A., Phillips, R. J., Solomon, S. C., Watkins, M. M., Wieczorek, M. A., and Williams, J. G., "Gravity Recovery And Interior Laboratory (GRAIL) Mission: Status At The Initiation Of The Science Mapping Phase," *Proc. Lunar and Planetary Science Conference*, Houston, TX, USA, March 19–23, 2012.
- ⁴Zuber, M. T., "Overview and First Science Results from the GRAIL Mission," *Proc. NASA Lunar Science Forum*, NASA Ames Research Center, Moffett Field, CA, USA, July 17–19, 2012.
- ⁵Roncoli, R. B. and Fujii, K. K., "Mission Design Overview for the Gravity Recovery and Interior Laboratory (GRAIL) Mission," *Proc. AIAA Guidance, Navigation, and Control Conference*, Toronto, Ontario, Canada, Aug. 2–5, 2010.